

Article

Pysanka-Inspired Electrode Modification with Aptamer Encapsulation in ZIF-8 for Urine Creatinine Electrochemical Biosensing

Antra Ganguly [†] , Anirban Paul [†]  and Shalini Prasad ^{*} 

Department of Bioengineering, University of Texas at Dallas, Richardson, TX 75080, USA; antra.ganguly@utdallas.edu (A.G.); anirban.paul@utdallas.edu (A.P.)

* Correspondence: shalini.prasad@utdallas.edu

[†] These authors contributed equally to this work.

Abstract: Drawing inspiration from the several thousand beautiful Pysanky egg art of Ukraine, we have developed a novel material, Aptamer–Gold Nanoparticles (AuNPs)@ZIF-8, that can be used for building sensitive and highly stable POC biosensors for longitudinal health mapping. Here, we demonstrate a sensitive and specific novel electrochemical biosensor, made of a novel synthesized in situ encapsulated aptamer–AuNPs@ZIF-8 composite, for monitoring levels of creatinine (0.1–1000 µg/mL). In this work, we have reported the synthetic protocol for the first-of-a-kind in situ encapsulation of aptamer and AuNPs together in a ZIF-8 matrix, and explored the characteristic properties of this novel material composite using standard analytical techniques and its application for biosensor application. The as-synthesized material, duly characterized using various physicochemical analytical methods, portrays the characteristics of the unique encapsulation strategy to develop the first-of-a-kind aptamer and AuNP encapsulation. Non-faradaic Electrochemical Impedance Spectroscopy (EIS) and Chronoamperometry were used to characterize the interfacial electrochemical properties. The biosensor performance was first validated using artificial urine in a controlled buffer medium. The stability and robustness were tested using a real human urine medium without filtration or sample treatment. Being versatile, this Ukrainian-art-inspired biosensor can potentially move the needle towards developing the next generation of sample-in-result-out robust POC diagnostics.

Keywords: encapsulated ZIF-8; metal–organic framework biosensor; art-inspired chemosensor; Pysanky biosensor point-of-care (POC) technology; electrochemical creatinine POC; creatinine aptamer chemosensor



Citation: Ganguly, A.; Paul, A.; Prasad, S. Pysanka-Inspired Electrode Modification with Aptamer Encapsulation in ZIF-8 for Urine Creatinine Electrochemical Biosensing. *Chemosensors* **2023**, *11*, 557. <https://doi.org/10.3390/chemosensors11110557>

Academic Editors: Jean-Francois Feller and Marco Frasconi

Received: 19 September 2023

Revised: 29 October 2023

Accepted: 31 October 2023

Published: 6 November 2023



Copyright: © 2023 by the authors. Licensee MDPI, Basel, Switzerland. This article is an open access article distributed under the terms and conditions of the Creative Commons Attribution (CC BY) license (<https://creativecommons.org/licenses/by/4.0/>).

1. Introduction

We are moving towards a world of personalized and preventive healthcare and preemptive therapeutics [1]. In this regard, self-monitoring point-of-care (POC) health monitors are saving the day by making routine home-based screening and overall personalized longitudinal health tracking possible. Via longitudinal monitoring of metabolic patterns, chronic disease trajectories and therapeutic efficacy can be reliably mapped [2]. To achieve the holistic and dynamic recording of a patient's health status over long periods using POC biosensors, advancements in the robustness and long-term operational stability of the sensing elements are critical. To succeed in longitudinal biomarker monitoring applications, stability factors such as longer shelf-life and reusability of the POC biosensors must be improved [3]. For long-term monitoring, not only must the stability of the biorecognition element be sustained, but the sensitivity of the capture probe should not decline over time [4]. In this context, regenerative biosensors have been reported in the literature, which reset the biosensor to its initial state. However, they face a significant challenge in that the regeneration chemistry is unique for a given analyte–capture probe and cannot be used to build versatile, “one-size-fits-all” formats [4]. However, in the non-regenerative

or “accumulative” mode, the target biomarker keeps accumulating on the capture-probe surface post-binding, resulting in reduced sensitivity over time.

Nanomaterial-based biosensors are gaining traction to retain high sensitivity, resolution, and wider detection ranges for long-term use [5,6]. Operating in the nanoscale realm affords higher surface area to volume ratios and macromolecular crowding effects for enhanced capture of target analytes and improved sensor metrics, especially for building miniaturized dynamic health-monitoring electrochemical POC diagnostics [7]. Owing to their attractive and exceptional properties, metal–organic frameworks (MOFs) are being used as transducers or recognition elements [8] for building diagnostic nano-biosensors for high sensitivity, enhanced operational stability, and long shelf life. A metal–organic framework, also known as MOF, is a hybrid material with high crystallinity made of mainly inorganic metal ions associated with an organic ligand via self-assembly. The term MOF was coined by Prof. Omar Yaghi in the 1990s at UC Berkeley, and since then, this field has grown rapidly [9–11]. Three-dimensional (3D) MOFs are fascinating clusters with unique sizes, shapes, and physicochemical properties. Among the various 3D MOFs reported in the literature, the use of Zinc-Imidazole Framework 8 (ZIF-8) is widespread among the scientific fraternity due to its exclusive structural and physicochemical properties [12,13].

ZIF-8 possesses many unique structural properties, but its most distinctive property is its unique pore size which allows this host molecule to accommodate guest nano or even macro molecules within itself. ZIF-8 possesses inherent porous cavities having a diameter of roughly 12 Å. It also possesses a narrow aperture of ~3.4 Å, allowing guest molecules to be absorbed and encapsulated [14]. This makes it suitable for a wide array of applications, such as gas storage [15], chemical separation [16], catalysis [17], sensing [18], and drug delivery [19]. The encapsulation of different hybrid materials within ZIF-8 enables enhanced sensing (catalytic, optical, electrochemical, conductive) properties as compared to the bare ZIF-8 (with no encapsulation) [20]. The hybrid composite, which is composed of guest species such as nanoparticles and biomolecules encapsulated inside the ZIF-8 matrix, has multiple advantages. One such advantage is its ability to protect the guest species from external stimuli. This phenomenon occurs due to the unique pore size of ZIF-8, which can accommodate the host species of any size into its designated cavity, thus being stabilized upon encapsulation. The in situ encapsulation of nanoparticles into ZIF-8 creates homogeneous phases and properties, resulting in sensitive electrochemical biosensors for longitudinal monitoring applications. ZIF-8 salts are highly soluble in water, whereas a ZIF-8 molecule is highly insoluble in water, and hence, during formation, it uptakes both water-soluble and insoluble species into its pristine cavity [21–24]. In this way, the guest molecules are also protected from solvation, which ultimately increases the shelf life of the composite or probe in a way. Metal nanoparticles (such as gold nanoparticles AuNPs) are popular for encapsulation in ZIF-8 frameworks for building electrochemical biosensors for two key reasons: (1) AuNPs possess a high surface-to-volume ratio, which decreases the electron tunneling distance, thereby enhancing electron transfer; (2) these species are highly conductive in nature, increasing the conductivity of the active surface; hence the output at the electrode–electrolyte interface supports a decent amount of electron transfer, resulting in a high-throughput sensor response.

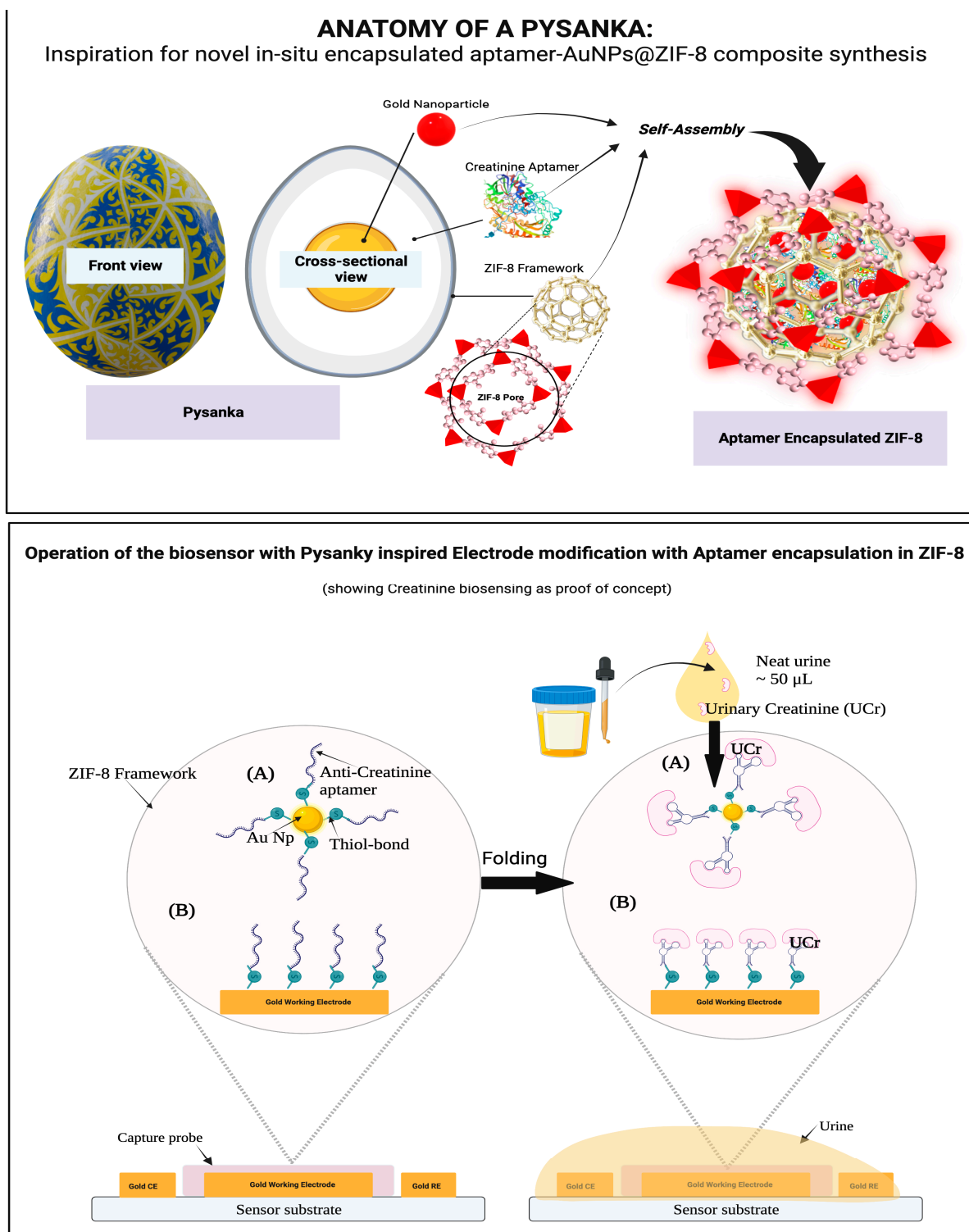
In this paper, we have leveraged the appealing physicochemical properties of the synthesized MOF material for building a novel biosensor. For this, we turned to the traditional art of Pysanky making from Ukraine. Pysanky (singular: pysanka) is the art of decorating Ukrainian Easter eggs with ornate floral patterns and symbolic geometric designs, which are considered harbingers of peace. Drawing inspiration from this age-old tradition, we have synthesized the first-of-a-kind ZIF-8 hybrid composite towards the development of a novel biosensor using aptamer-encapsulated ZIF-8 material for electrode modification for enhanced electrochemical sensing. We chose creatinine as our target proof-of-concept biomarker of interest. This scheme is versatile, and the application of the developed material can be extended for biomarker detection and quantification schemes for monitoring and managing other diseases. Creatinine is an important metabolic

biomarker involved in several physiological processes, including muscle and protein metabolism, and is the most important biomarker for mapping kidney health and the longitudinal assessment of renal function [25–32]. The healthy range of creatinine in urine has been reported to be 4.4–18 mM [32,33]. The conventional methods of creatinine detection are based on chromatography or enzyme-based methods, which often suffer from complex sample preparation, low specificity, low reliability, and low stability [34,35]. Hence, novel approaches based on nanotechnology and nanomaterials are being extensively studied to build creatinine biosensors to overcome these limitations [36–38]. Table S1 in the supplementary information discusses the creatinine biosensors in the recent literature and compares their performance based on detection range, specificity, and limit of detection.

Scheme 1 draws parallels between the structure of traditional Pysanky making and our novel material. Pysanka art is made by taking an egg and creating patterns on the eggshells by melting wax on the surface and coloring layer by layer, creating an outer hydrophobic/water-resistant design on the surface.

For our synthesized material, the outer ZIF-8 MOF layer acts as this extremely hydrophobic shell/cage that holds the contents in without letting them leak out (similar to an eggshell, which contains the yolk and the albumin). Analogous to the egg yolk is that the gold nanoparticle acts as the core and is bound to the highly specific anti-creatinine aptamer (similar to the albumin layer) via strong thiol bonds.

Scheme 1 also describes the operation of our biosensor, which is essentially a planar three-electrode electrochemical system with a gold measurement electrode. A layer of the gold nanoparticle and anti-creatinine aptamer encapsulated ZIF-8 complex is used to modify the working electrode. This encapsulated MOF results in a hybrid capture probe where the anti-creatinine aptamer lends it high specificity and the nano-porosity of the MOF layer and the gold nanoparticles provide high sensitivity and operational stability. The aptamer is thiol-modified to achieve strong thiol bonds with the gold nanoparticles [39]. Instead of using any enzymatic approach, we have used an aptamer to avoid the multi-step reaction (Jaffe's Method) for ease of long-term use and no sample preparation at the user end. Aptamers are superior in terms of dealing with harsh environments (such as urine) and show higher selectivity and greater pH and thermal stability and are sometimes called "synthetic antibodies" [40]. Hence, an aptamer has been chosen over a traditional anti-creatinine antibody for creatinine sensing in this work. When a drop of unfiltered and unprocessed urine (<100 μ L) is dispensed onto the sensor surface, the creatinine molecules eluted in the urine selectively enter the MOF cage, owing to size-based sieving, which prevents bulky interferents such as contaminants and proteins from reaching the sensor surface. Upon interacting with creatinine molecules, the aptamer undergoes a conformational change, resulting in the modulation of the electrical properties at the electrode–urine buffer interface. An AC-based method of Electrochemical Impedance Spectroscopy and a DC-based method of Chronoamperometry were used to capture these effects to calibrate the sensor [41,42]. The sensor operates in non-faradaic mode and does not require additional redox tags for signal amplification for reliable sensing [43,44].



Scheme 1. Schematic showing the development of our sensitive and specific novel electrochemical biosensor made of a novel synthesized in situ encapsulated aptamer-AuNPs@ZIF-8 composite using a traditional Ukrainian Pysanka as a model. The figure also shows the elements and operation for urine creatinine biosensing. (A) shows the anti-creatinine aptamer attached to the gold nanoparticle encapsulated within the ZIF-8 framework and (B) shows the anti-creatinine aptamer attached to the planar gold working electrode via strong thiol bonds. When the sample containing expressed creatinine molecules is introduced to the working electrode, the aptamer folds and changes its conformation to capture the creatinine molecules, resulting in interfacial modulation for electrochemical biosensing.

2. Materials and Methods

Analytical grades of Zinc Nitrate and 2-Methylimidazole were purchased from Sigma-Aldrich and used without further purification. Chemicals such as methanol procured from Sigma-Aldrich were also used without further purification. The synthesis of the Apta-AuNP@ZIF-8 nanocomposite was performed in aqueous media at room temperature. The thiolated anti-creatinine aptamer was purchased from Creative Biolabs (Shirley, NY, USA). The aptamer sequence obtained from the vendor was:

5'-CGACGGTGGCCTATTAATAGCTTTAGTTTAAGAAAAGTAATAGGGGGTGTTCG-3'

Real pooled human urine (PHU) samples were procured from Lee Biosolutions (St. Louis, MO, USA). The samples were aliquoted and stored at -20°C . The samples were thawed and centrifuged before use. The supernatant solution was used for the biosensing experiments. To prepare the synthetic/artificial urine samples, the protocol for MP-AU discussed by Sarigul et al. [45] was used. A Metrohm 220 AT three-electrode (gold working and counter electrodes and silver reference electrode) screen-printed sensor (Metrohm USA, Herisau, Switzerland) was used for the electrochemical experiments, and the working electrode was modified using the prepared ZIF-8-based nanocomposite solutions for testing.

2.1. Synthesis of Apta-AuNP@ZIF-8 Nanocomposite

The synthetic route of Apta-AuNPs @ZIF-8 is being followed from our previous synthetic experiment where we have successfully encapsulated nanomaterial into a ZIF-8 matrix, but the encapsulation of biomolecules like aptamer along with AuNPs, and the formation of Apta-AuNP@ZIF-8, is a completely novel material, as per our knowledge. To synthesize aptamer-AuNps encapsulated ZIF-8 using an in situ encapsulation strategy, we have taken two separate solutions: Zinc Nitrate (Solution A) and 2-Methylimidazole (Solution B). The concentration of zinc nitrate is optimized to be 8 mM by weighing 2.38 g and dissolving it in 60 mL of methanol solution. We added 10 μM and 1 mL of the aptamer to solution A. The addition of aptamer into solution A results in the solution turning pale yellow visually. On the other hand, to prepare solution B, 2-methyl imidazole was weighed at 2.628 gm to prepare a 30 mM solution in 20 mL of methanol. This resulting solution also turns pale yellow from transparent. Both solutions are stirred at 400 rpm at room temperature to ensure the complete dissolution of the species into the solvent. The gold nanoparticles used in this work are purchased commercially, having a concentration of 0.1 mg/mL and an average size of 10 nm, from Alfa Aesar (USA). Prior to its use, we probe-sonicated 10 mL of AuNPs for one hour and directly added it to solution B. Both separately prepared solutions, A and B, were then mixed together in a 250 mL beaker and stirred at 6000 rpm at room temperature for at least 10 h. The beaker was covered using aluminum foil to avoid any evaporation of solvents. The solution turns opaque from transparent in 15 min, indicating the formation of the nanocrystalline composite by in situ encapsulation of aptamer and AuNPs into ZIF-8. The resulting mixture was then set aside for settling after 10 h, and a thick layer of precipitation, slightly pink in color, was observed. The color detected by the naked eye gave a glimpse that AuNPs were successfully encapsulated along with the aptamer. However, the supernatant was found to be almost transparent, depicting most of the guest species had been encapsulated into the host species. The precipitation was then separated out slowly and carefully and washed with DI water five times using centrifugation at 6000 rpm. This intense washing step helped remove all the water-soluble unreactive and unencapsulated species, and we collected 10 mL of supernatant each time we washed to check the impurities. After the final washing process, the composite was resuspended in methanol, and the final product was stored in a glass vial and further stored in a vacuum oven at room temperature to avoid any moisture.

2.2. Electrode Preparation and Electrochemical Methods

All the Electrochemical Impedance Spectroscopy (EIS) and Chronoamperometry (CA) experiments were performed using a Gamry Reference 6000 potentiostat (Gamry Instruments, PA, USA). For EIS, the impedance response for a wide frequency range of

1 Hz–1 MHz was studied for an input voltage of 10 mV (RMS) applied at the working electrode. For CA experiments, -0.5 V was applied at the working electrode for 30 s, and the data was collected at $t = 0.01$ s. The impedance and current values for EIS and CA, respectively, were collected and compared to those for the blank or zero doses (zero creatinine analyte concentration). The sensor was calibrated for a broad range of 0.1–1000 $\mu\text{g}/\text{mL}$ of creatinine for both artificial and real pooled human urine for both EIS and CA.

2.3. Statistical Analyses

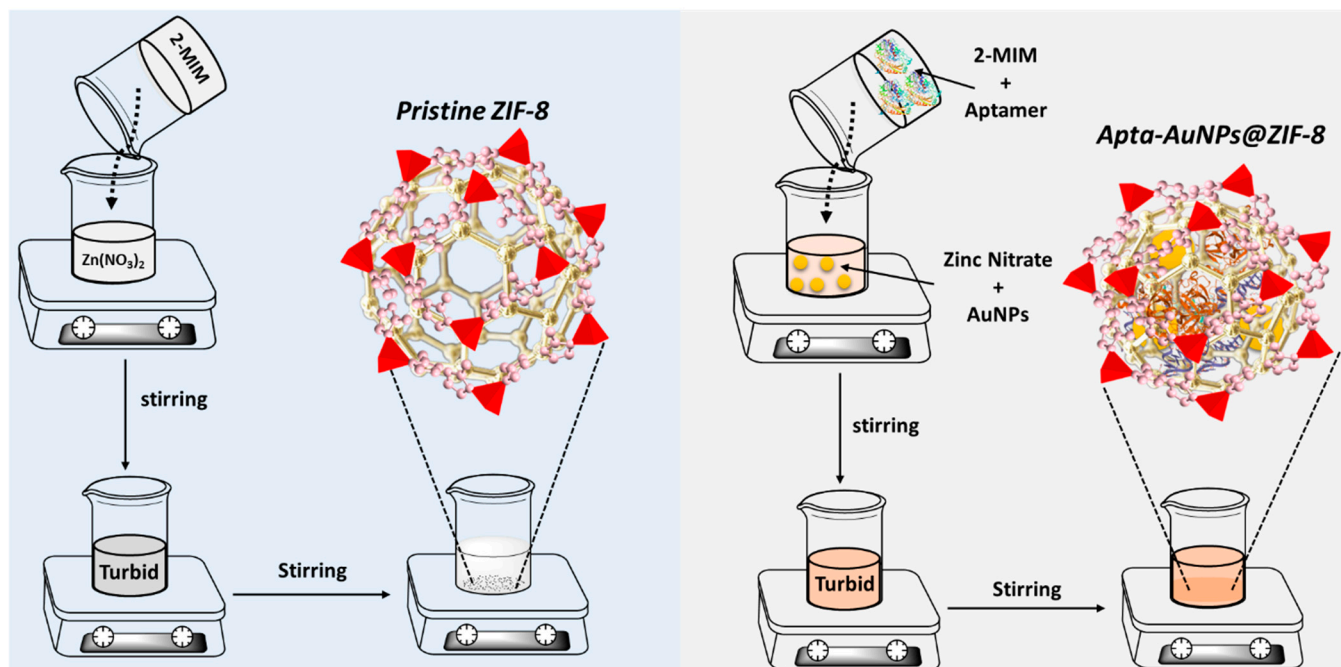
Graph Pad Prism version 9.5.0 (GraphPad Software Inc., La Jolla, CA, USA) was used to perform and visualize all the statistical analyses. ns: non-significant, * $p < 0.05$, ** $p < 0.01$, *** $p < 0.001$, **** $p < 0.0001$. Data have been represented as mean \pm standard error of mean (SEM) for all replicates ($n = 3$ inter-sensor and $n = 3$ intra-sensor replicates). An unpaired two-sided Student's t -test analysis with $\alpha = 0.05$ was used for testing significance between the specific-signal and non-specific-signal response groups. A 4-PL non-linear regression was conducted to fit the calibration dose–response curves.

3. Results and Discussion

There are multiple ways in which composite materials can be synthesized, and one of the popular and conventional ways to achieve this is by mixing multiple species. There are many advantages to such a method for obtaining composite species, but one of the disadvantages is the formation of heterogeneous phases, which are sometimes not suitable for particular applications, especially for our case. New strategies such as in situ encapsulation have evolved, which provide a high degree of freedom towards optimization of the architecture of the composite species, such as obtaining a homogenous phase which is helpful for electrochemical sensor development. The solubility of ZIF-8 or modified ZIF-8 has its own pros and cons. As mentioned before, the pre-synthetic salts are highly water soluble, although the synthetic species is highly hydrophobic. The insolubility of this species can be utilized in a different way, where the guest species is likely to be avoided, being soluble in water, and hence can operate in aqueous media with an enhanced shelf life. As the in situ encapsulation of guest species into the ZIF-8 moiety is still under active research, understanding and tuning the pore size of ZIF-8 to allow such a phenomenon to occur is highly sensitive and requires intensive optimization, or else the post-synthetic composite suffers adverse defects. Hence, the physicochemical characterization of such synthesized species is inevitable. We have explored the physical aspects of the material using diffractometry, thermogravimetry, and microscopy techniques, whereas the chemical property has been evaluated using FTIR and UV-Vis. The goal behind all these characterizations is mostly to confirm the encapsulation of guest species into the host molecule. Moreover, the electrochemical characterization we have explored is also equally important for us from an application point of view.

The novel synthesized nanomaterials ZIF-8, AuNP@ZIF-8, and Apta-AuNPs@ZIF-8 show distinct material properties duly captured using various physicochemical techniques. Among these three isomorphs, our interest lies mainly in Apta-AuNP@ZIF-8 for application purposes. Thorough characterizations have been implemented to understand the encapsulation of guest species and the effect of the native framework upon encapsulation. We have also investigated their inherent morphologies using high-power electron microscopes to fully unlock the features of such materials. As mentioned earlier, in situ encapsulation has a strong advantage in fabricating composite materials of particular interest, and in our case, it is for electrochemical sensing. The conventional mixing of multiple species can end up with agglomeration and the creation of multiple heterogeneous phases, which are not suitable for developing a suitable probe or, more technically, a transducer for electrochemical sensor application. The in situ encapsulation strategy includes the encapsulation of guest species upon the simultaneous formation of the host composite. For this case, we have chosen aptamer and gold nanoparticles as guest species, which have been in situ encapsulated into the ZIF-8 matrix in a synthetic mixture where the formation of the framework is directly

associated with the nature of the guest species ready to be encapsulated. This strategy provides a homogenous phase of composites where most of the physical properties are dominated by ZIF-8 only, but its transduction ability has become highly improved due to the back-end support of the encapsulated guest species. The encapsulation approach has been depicted using a schematic figure for better clarity, depicted in Scheme 2.



Scheme 2. Schematic illustration of the synthetic route for preparing bare ZIF-8 and encapsulated ZIF-8 [25].

3.1. Powder X-ray Diffraction

P-XRD has been performed for all three synthesized materials to characterize their phases. All samples are vacuum dried before performing P-XRD. The P-XRD result has been depicted in Figure 1a, which includes the phases of three distinct MOF materials: ZIF-8 (designated as red line), AuNP@ZIF-8 (designated as blue line), and the most important: Apta-AuNP@ZIF-8 (designated as black line). All of the significant and fingerprint phase angles of the parent ZIF-8 (JCPDS 00-062-1030) have been found present in all of its three encapsulated isomorphs and clearly overlap with more than 95% peak matching. This observed pattern of P-XRD of all these three species depicts no change in the native MOF architecture. This phenomenon is not quite new, as a similar pattern has been found when encapsulating guest species into the MOF matrix. Pristine ZIF-8 is not a new material, and several studies have been conducted based on its pore size and aperture. The literature suggests that ZIF-8 possesses a fairly moderate pore size of about 12 Å and a formal aperture of nearly 3.5 Å, whereas it has also been found that the aperture window can be extended up to 7 Å and even more to accommodate guest species. The interesting fact is the encapsulation of a large biomolecule: An aptamer, in this case, depicts variable structural artifacts of native ZIF-8. The result also does not show any distinguishing P-XRD peaks of either gold nanoparticles or aptamer, probably due to the masking effect of the strong PXRD response of ZIF-8 itself. The obtained pristine ZIF-8 peaks are matched with simulated standard ZIF-8 (JCPDS 00-062-1030; $a = b = c = 17.0116 \text{ \AA}$ $\alpha = \beta = \gamma = 90^\circ$), and we have found an exact match, depicted in Supplementary Figure S1, which suggests the in situ encapsulation of guest species cannot hamper the crystallinity of the host ZIF-8 architecture. This observation suggests that the as-synthesized ZIF-8 powder is pure in nature and remains intact while encapsulating AuNPs and aptamer.

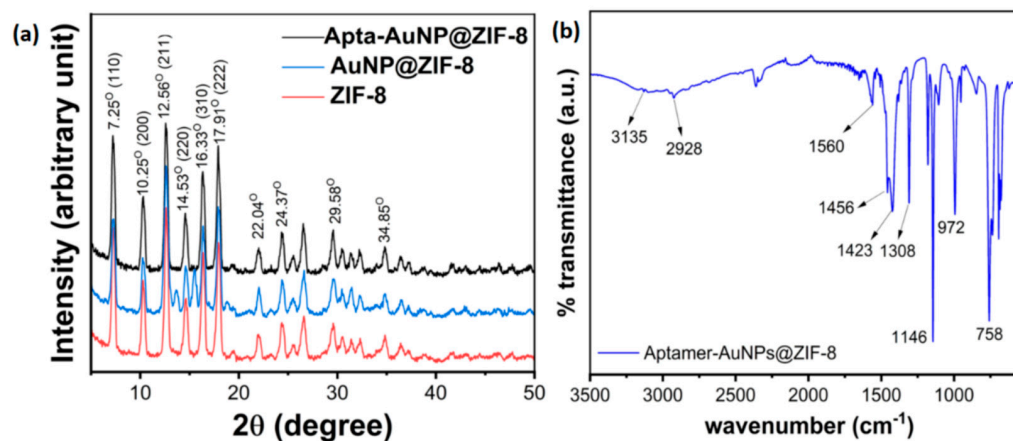


Figure 1. (a) P-XRD patterns of ZIF-8 (red), AUNP@ZIF-8 (blue), and Apta-AuNP@ZIF-8 (black) show distinct P-XRD peaks. (b) ATR-FTIR spectrum showing characteristic peaks of the gold nanoparticle and creatinine aptamer encapsulated ZIF-8 compound.

3.2. Fourier Transform Infrared Spectroscopy

The chemical structure of the as-synthesized Apta-AuNP@ZIF-8 was characterized using Fourier Transform Infrared (FT-IR) spectroscopy to analyze the interaction and encapsulation of aptamer and AuNPs inside ZIF-8. FT-Infrared (IR) spectroscopy was performed using a Nicolet iS-50 FTIR (Thermo Scientific Inc., Waltham, MA, USA) in Transmittance mode. The IR spectra were collected using Germanium crystal for 256 scans at a resolution of 4 cm⁻¹ in the wavelength range 500 cm⁻¹ to 4000 cm⁻¹. Three samples were analyzed by directly putting the powdered form of Apta-AuNP@ZIF-8 on the crystal and running the scan. The IR spectra so obtained are depicted in Figure 1b, where the FTIR spectra of the as-synthesized species are depicted by the blue line. Several fingerprint peaks of pristine ZIF-8 are found to be present in AuNPs@ZIF-8 and Apta-AuNPs@ZIF-8. As such, 3135 cm⁻¹ depicts the aromatic C-H asymmetric stretching vibrations of ZIF-8, whereas the peak at 1585 cm⁻¹ depicts the C=N stretching vibration, 1456 cm⁻¹ depicts entire ring stretching, and 1146 cm⁻¹ depicts the aromatic C-N stretching mode of pristine ZIF-8. Also, the peaks obtained at 972 cm⁻¹ and 758 cm⁻¹ accounted for C-N bending vibrations and C-H bending modes, respectively. The result depicts that the fingerprint FTIR peaks of pristine ZIF-8 are present in Apta-AuNPs@ZIF-8, and depicts that the pristine ZIF-8 backbone is still chemically active and, due to high abundance of the host species, it masks the chemical property of the guest species, which is actually helpful for this application as the role of the guest species in this composite is to enhance the signal output (role of AuNPs) and engage biochemical interaction (role of aptamer) upon encapsulation into the ZIF-8 motif.

3.3. Scanning Electron Microscopy Elemental Mapping (SEM)

The morphology of the as-synthesized materials has been investigated using FE-SEM. The samples are crushed well using a mortar and pestle and vacuum-dried overnight before performing FE-SEM. The FE-SEM result of Apta-AuNP@ZIF-8 has been depicted in Figure 2. Figure 2a,b represent a zoomed-out view at 10 microns depicting the basic morphology of the as-synthesized Apta-AuNP@ZIF-8, and the result depicts a distinct homogeneous formation of cubic crystals. Upon zooming into a single crystal at a magnification of 5 microns in Figure 2c and 1 micron in Figure 2d, it is quite clear that the as-synthesized material possesses a cubic crystal structure having an edge length of almost $a = b = c$. The result also correlates with the outcome of P-XRD characterization. It is quite confirmed from the FESEM results that the encapsulation of AuNPs and aptamer does not deform the native structure of ZIF-8.

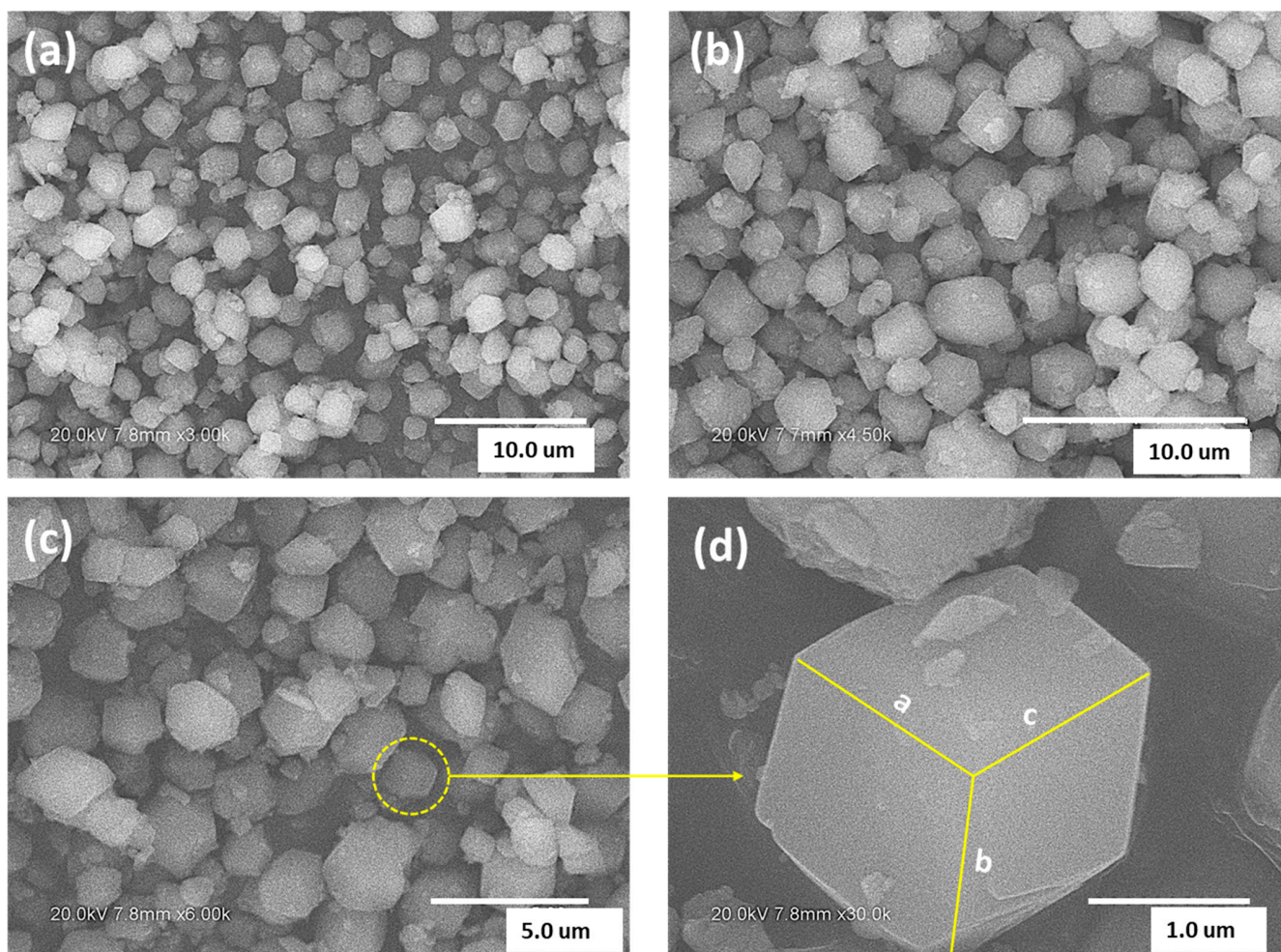


Figure 2. (a,b) FE-SEM of Apta-AuNP@ZIF-8 at a magnification of 10 microns showing distinct homogeneous crystals having a shape almost like cubes. (c) Morphology captured at a resolution of 5 microns shows the presence of many crystal cubes; some are perfectly cubic, and some are deformed. (d) This shows the morphology of a particular cubic crystal captured at 1 micron showing an almost-cubic crystal having edge length $a = b = c$.

Moreover, as seen in the FE-SEM images, different types of crystals with different morphologies have been observed, but if we look closely, most of the crystal morphology is either cubic or deformed cubic, which is rhombohedral. The reason for such variety depicts the nature of the encapsulation reaction, which is a very quick in situ transformation, and the morphology of the hybrid composite is mostly governed by the pristine ZIF-8. To understand this artifact more vividly, we have performed FE-SEM of all three isomorphs at the same magnification of 1 micron and put them side by side for comparison. The result is depicted in Figure 3. The result shows that ZIF-8 has an almost cubic crystal morphology and depicts its native morphology, duly supported by the literature. While encapsulating AuNPs, the native cubic morphology is found to be deformed, probably due to accommodating AuNPs inside the MOF matrix. The interesting fact is that, when AuNPs and aptamer are both encapsulated, the encapsulated MOF retains its native cubic morphology. This outcome points out the structural aspect of ZIF-8 upon post-encapsulation and suggests that AuNPs and aptamer, while present together, increase the host-guest interaction, resulting in the deformed morphology regaining the native framework architecture.

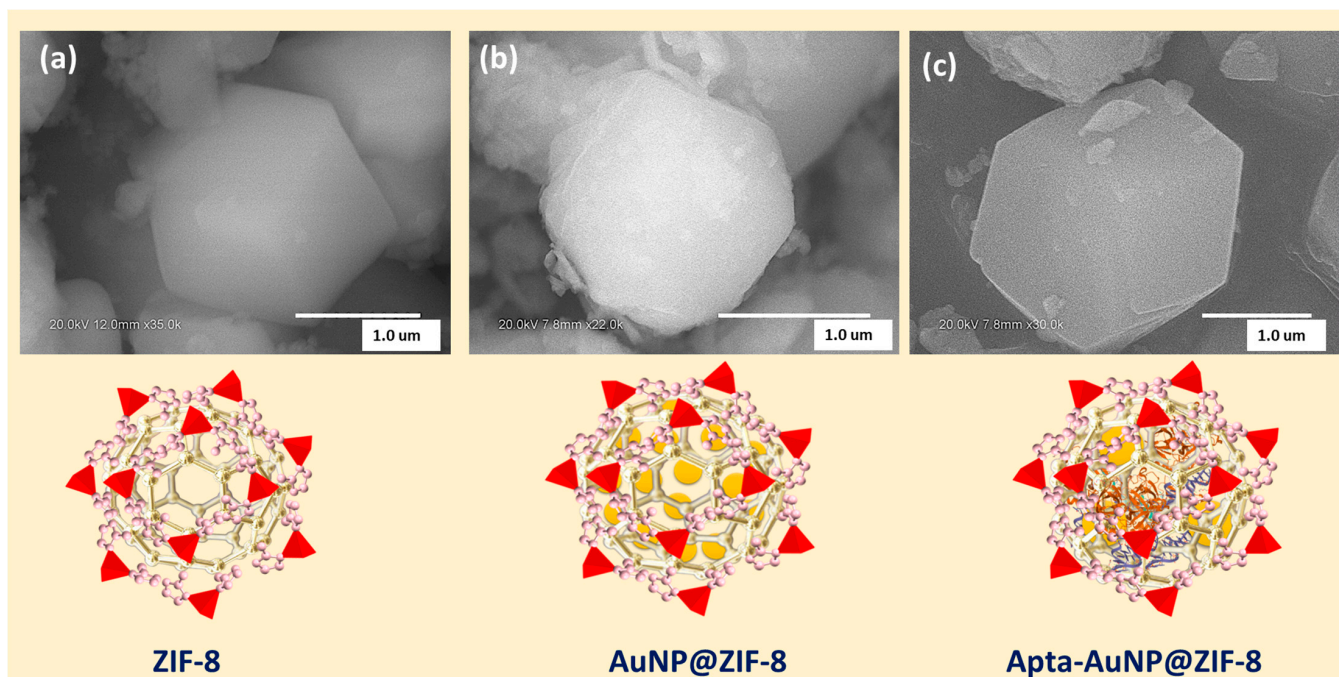


Figure 3. Side-by-side comparison of the morphology of ZIF-8 isomorphs upon encapsulation at the same magnification depicts distinct structural features.

3.4. Transmission Electron Microscopy (TEM)

To understand the three-dimensional morphology of the as-synthesized novel material Apta-AuNP@ZIF-8, we have performed HR-TEM, and the result is depicted in Figure 4. Figure 4a depicts the morphology at a higher magnification of 0.2 μM , showing the hexagonal shape of the synthesized crystal, which perfectly correlates with the FE-SEM result, having the cubic crystal morphology. Figure 4b depicts the dark-phase TEM output of the material, which suggests the presence of an organic moiety as well as metal fringes, obvious for the metal presence of zinc and gold nanoparticles. Upon further magnification at 5 nm, substantial fringes have been found, depicting the presence of Zn and AuNPs and presented in Figure 4c. Figure 4d depicts the presence of gold fringes having a fringe gap of 0.24 nm, depicting the Au (111) plane perfectly matching the P-XRD result. As the presence of AuNPs is very scant in the whole composite, this defends the hypothesis of the encapsulation of AuNPs and aptamer into the ZIF-8 matrix.

3.5. Atomic Force Microscopy (AFM)

We have also performed AFM to observe the topology of the synthesized Apta-AuNP@ZIF-8, and the result is depicted in Figure 5. The result depicts the unique topology of the as-synthesized species showing cubic crystal homogeneous topology duly correlated with the FE-SEM results.

Figure 5a depicts a 2D depiction of the topology of Apta-AuNP@ZIF-8, whereas Figure 5b depicts a 3D topology of Apta-AuNP@ZIF-8 having an average depth profile of 0.6–0.7 μM , suggesting the formation of a homogeneous crystalline heterostructure. This also suggests that the in situ encapsulation of guest molecules does not rupture the crystalline property of native ZIF-8, duly observed using other microscopy tools.

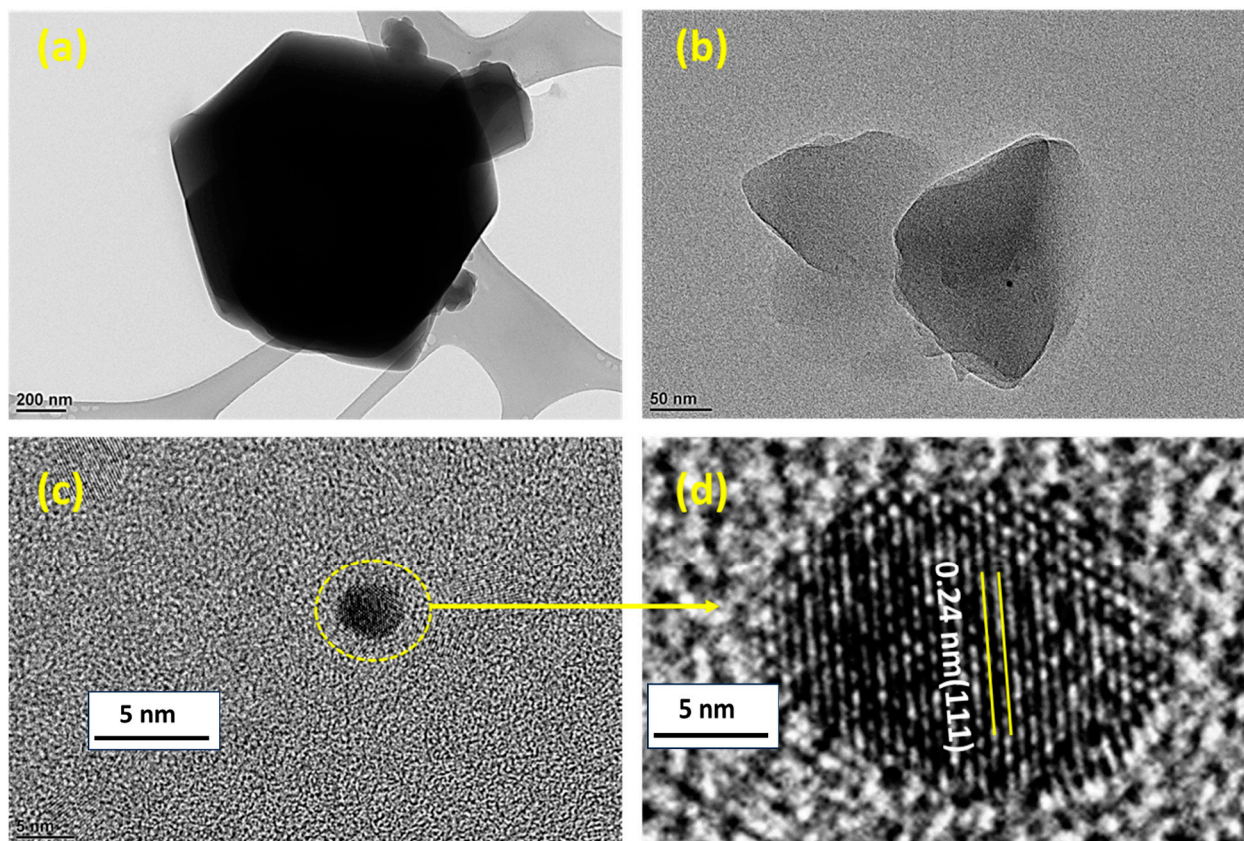


Figure 4. (a) Dark-phase TEM depicting the ZIF-8 crystal from a 3D spatial angle having a hexagonal architecture and portraying the ZIF-8 moiety at the 0.2 mM scale. (b) The contrast-phase diagram of ZIF-8 at 50 nm captures the presence of nano/sub-microparticles, portraying encapsulated molecules. (c) The presence of metal fringes upon zooming in to 5 nm depicts the probable presence of AuNPs. (d) A fringe gap of 0.24 nm attributed to the Au (111) plane confirms the presence of AuNPs.

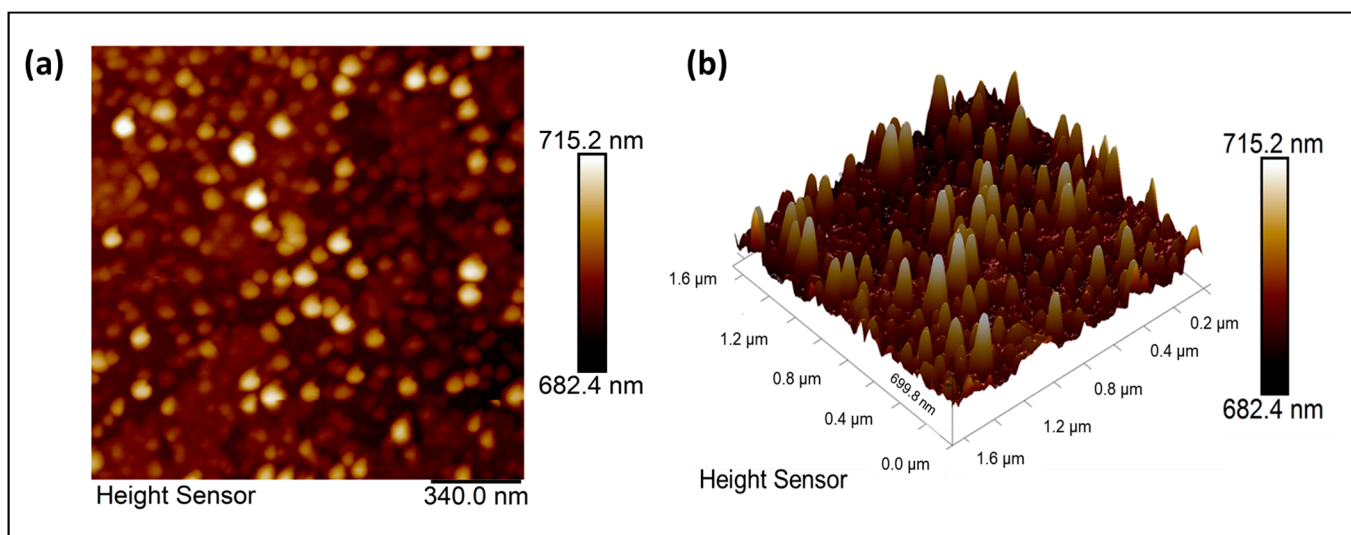


Figure 5. (a) 2D AFM topology of Apta-AuNPs@ZIF-8 depicts homogenous crystallinity and a smooth depth profile. (b) 3D AFM of the synthesized material depicts a homogeneous height profile between 0.68 mM and 0.71 mM.

3.6. Thermogravimetric Analysis

To check the thermal stability of all the synthesized species, we have performed TGA for all the samples, and the result is depicted in Supplementary Figure S2. The result shows the blue line corresponding to Apta-AuNP@ZIF-8, whereas the red line corresponds to AuNP@ZIF-8, and the black line corresponds to ZIF-8. All the isomorphs show almost similar thermogravimetry trends where a kink at 200 °C corresponds to the breakdown of a long-chain carbon backbone, probably corresponding to the breakdown of the aptamer chain encapsulated into the ZIF-8 matrix, whereas MIM bridging ligand decomposition is observed at 350 °C and a plateau is obtained after that, which designates the relatively high thermal stability of these as-synthesized materials.

3.7. UV-Vis Spectroscopy

Moving from physical characterization to chemical characterization, UV-Vis has been performed to characterize the gold nanoparticle and the UV-Vis effect of the as-synthesized material. The result is depicted in Supplementary Figure S3, which shows the fingerprint peak of a AuNP at 520 nm and depicts the synthesis of a AuNP in its pure form. The UV-Vis results of all synthesized materials, ZIF-8, AuNP@ZIF-8, and Apta -AuNP @ZIF-8, are also depicted in Figure 8. The result depicts a blunt peak at 416 nm, whereas there is no significant peak for the other two isomorphs in the visible region, indicating that the complete encapsulation of gold nanoparticles is getting masked by the ZIF-8 architecture.

3.8. Electrochemical Characterization

To calibrate the sensor for the quantification of creatinine levels in the test sample, an established electrochemical transduction technique of Electrochemical Impedance Spectroscopy (EIS) was used. Using this method, a small-signal AC voltage is applied at the working electrode to perturb the Electrical Double Layer (EDL) at the electrode–urine buffer interface [46,47]. A change in the electrical properties of this interface occurs in the form of a change in the dielectric constant due to creatinine binding to the ZIF-based capture probe and the rearrangement of water and ionic species at the EDL. When an AC voltage is applied at the EDL, it results in a phase-shifted current, the ratio of which is used to obtain the interfacial impedance as a function of binding [43], which is then correlated to the concentration of creatinine in the sample [41,42]. Additionally, Chronoamperometry (DC-based method) [41,42] was used for method validation for reliable creatinine biosensing.

The sensor was first calibrated for a wide dynamic range of 0.1–1000 µg/mL for urinary creatinine biosensing using a controlled artificial urine buffer medium (at median human urine pH of 6). Next, the sensor calibration was performed using pooled human urine samples (pH 6.5) to test the stability of the aptamer-encapsulated MOF capture probe in the real unfiltered and unprocessed urine sample. The *t*-test analysis in Figure 6a compares the sensor performance for both artificial and real human urine. A *p*-value > 0.05 is obtained, which validates that the sensor performance is stable and unaffected by the buffer microenvironment. A characteristic Bode phase plot (impedance phase angle versus the logarithm of frequency) shown in Figure 6b obtained from EIS analysis depicts the capacitive, non-faradaic mode of operation as evidenced by the negative phase angle values for the entire dynamic range (100 Hz which is chosen as the frequency of operation for EIS). The electrochemical behavior of the developed novel creatinine aptamer encapsulated ZIF-8 material was further studied as a Nyquist plot (an imaginary component of impedance on the Y-axis and real component of impedance on the X-axis), using a bare/un-encapsulated ZIF-8 as a control (Figure 7). From Figure 7, it is clear that the aptamer-encapsulated ZIF-8 material shows a specific and completely opposite dose-dependent trend compared to the control sample, i.e., bare ZIF-8 without any aptamer.

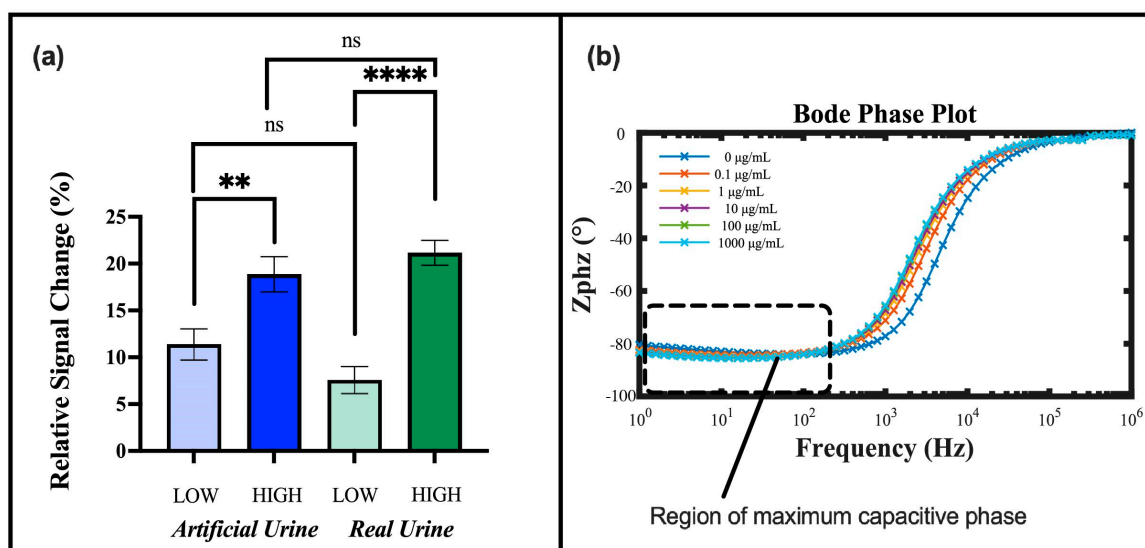


Figure 6. Electrochemical characterization of the sensitive and specific biosensor made of novel synthesized in situ encapsulated aptamer-AuNPs@ZIF-8 composite - (a) *t*-test comparison of sensor performance in artificial and real human urine, ns: non-significant, ** $p < 0.01$, **** $p < 0.0001$. (b) Bode phase plot showing the capacitive operation at 100 Hz for EIS studies for increasing creatinine doses.

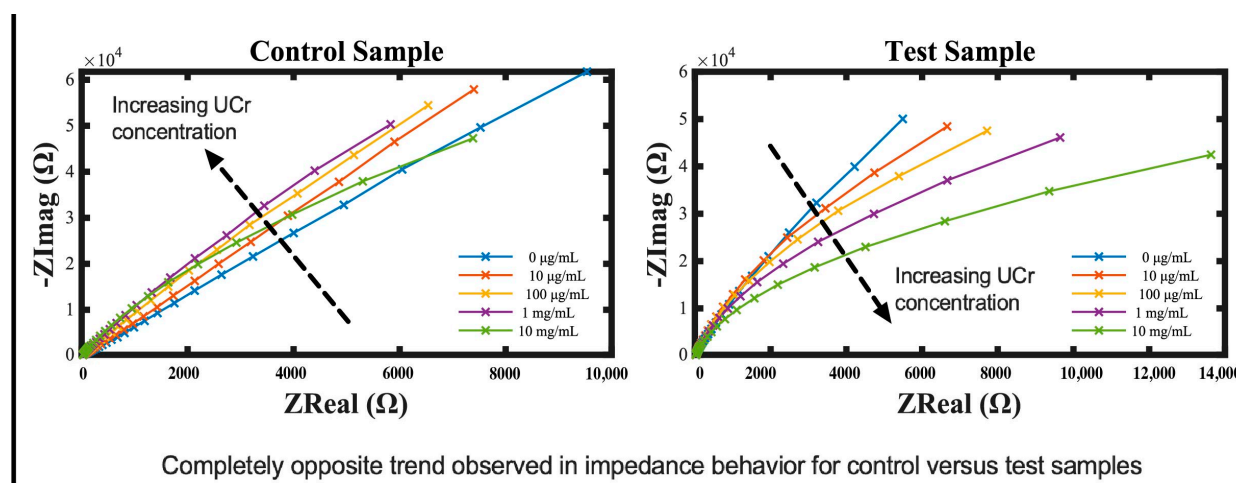


Figure 7. Electrochemical characterization of the sensitive and specific biosensor made of novel synthesized in situ encapsulated aptamer-AuNPs@ZIF-8 composite: Nyquist plots obtained from EIS for control (no aptamer) and test (anti-creatinine aptamer encapsulated ZIF-8) samples for increasing creatinine doses.

3.9. Electrochemical Sensor Performance

The modulus of impedance (Z_{mod}) was studied to obtain the calibration dose–response curves for quantifying the urinary creatinine levels using EIS. The Z_{mod} decreased in a dose-dependent manner, from the lowest to the highest doses at 100 Hz. For CA, the peak current at time $t = 0.01$ s was used for calibrating the sensor. A decrease in the peak current was observed with increasing creatinine doses. In this way, the electrochemical behavior of the sensor as a function of creatinine binding to the capture probe was analyzed using EIS and CA.

Figure 8a,b show the dose–response curves for creatinine in pooled human urine samples using EIS and CA, respectively. We observed a linear dose response for both real pooled human urine samples ($n = 3$) and the artificial urine samples ($n = 3$) over a

wide dynamic range of 0.1–1000 $\mu\text{g}/\text{mL}$ of creatinine for both EIS and CA methods. The modulus of the impedance measured at the EDL interface was observed to decrease as a function of dosing due to increasing interfacial capacitance as a result of creatinine binding to the ZIF-8–aptamer capture probe. Figure 8c,d show the relative changes in the Z_{mod} values relative to the blank (zero creatinine dose) baseline. To test for the sensor specificity and the effect of interfering species (also expressed in urine) on the sensor performance for creatinine detection, cross-reactivity studies using glucose and urea (1:1 volume by volume cocktail) were performed. As shown in Figure 8e,f, a p -value of <0.0001 obtained for both EIS and CA methods from Student's t -test analysis (unpaired, two-tailed, $\alpha = 0.05$) shows that there is a significant difference in sensor output for specific (urine creatinine) and non-specific (interferents) samples at the input. In this way, the sensor specificity was validated.

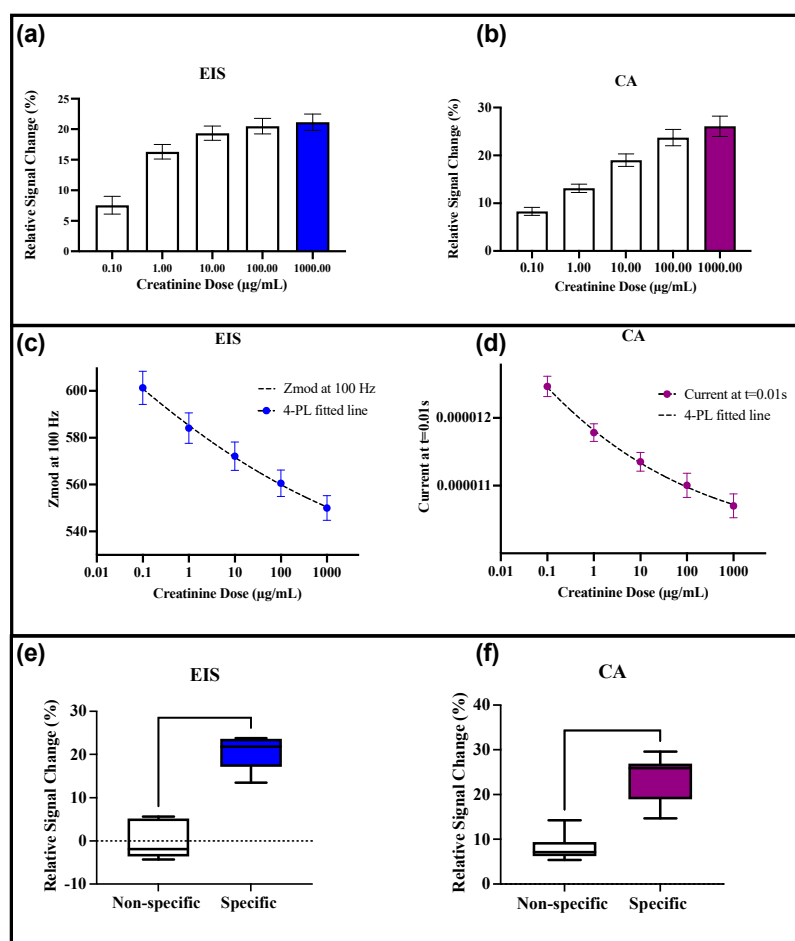


Figure 8. Absolute-value calibration dose–response curve using (a) EIS and (b) CA for pooled human urine samples. Baseline-relative calibration dose–response curve using (c) EIS and (d) CA for artificial urine samples. (e,f) show the t -test analysis results for cross-reactivity study or non-specific (glucose and urea) versus specific (creatinine) doses.

4. Conclusions

In this work, we discussed the development of a novel hybrid capture-probe material using a gold nanoparticle aptamer encapsulated ZIF-8 compound. The material synthesis was inspired by the traditional Pysanky art of Easter egg decoration in Ukraine. Extensive material analysis was performed using physical and chemical characterization methods. We also demonstrate the application of the developed MOF material towards electrode modification for non-faradaic electrochemical biosensing using two established electroanalytical methods, an AC-based method of Electrochemical Impedance Spectroscopy and a

DC-based method of Chronoamperometry. Using a combination of AC and DC techniques, subtle changes in the resistive and capacitive properties at the electrical double-layer interface were captured as a function of the binding of creatinine expressed in the test urine sample to the ZIF-8–aptamer capture probe. The sensitivity and specificity of the calibrated sensor were also discussed for a wide urinary creatinine range of 0.1–1000 µg/mL. These achievements highlight the unique potential of our novel synthesized material and the proposed sensing scheme to boost the performance of the current affinity of biosensors for POC applications. Future work will involve testing our novel synthesized in situ encapsulated aptamer-AuNPs@ZIF-8 composite for long-term operational stability and shelf-life enhancement of the traditional capture probes for longitudinal biomarker tracking studies.

Supplementary Materials: The following supporting information can be downloaded at: <https://www.mdpi.com/article/10.3390/chemosensors11110557/s1>, Figure S1: PXRD comparison of synthesized ZIF-8 and simulated ZIF-8 (JCPDS 00-062-1030) showing more than 95% peak matching depicting the purity of the synthesized ZIF-8; Figure S2: TGA comparative analysis of as-synthesized material having three distinct decomposition phases depicting rigidity and stability of the composite materials; Figure S3: UV-Vis characteristics of AuNPs showing peak at 520 nm and depicting the size of the AuNPs as 5 nm; Figure S4: Validation of signal enhancement due to Aptamer AuNP@ZIF-8 versus plain aptamer system; Table S1: Comparative table of current methods of creatinine detection.

Author Contributions: S.P., A.G. and A.P. conceived the project framework and designed the experiments. A.P. and A.G. designed and performed the experiments. A.G., A.P. and S.P. wrote the article. All authors have read and agreed to the published version of the manuscript.

Funding: This research received no external funding.

Institutional Review Board Statement: Not applicable.

Informed Consent Statement: Not applicable.

Data Availability Statement: The data presented in this study are available on request from the corresponding author.

Acknowledgments: The authors would like to thank Jiechao Jiang and Yi Shen of the Characterization Center for Materials and Biology at the University of Texas at Arlington for their help with the characterization experiments.

Conflicts of Interest: Dr. Shalini Prasad has a significant interest in EnLiSense LLC. (Allen, TX, USA), a company that may have a commercial interest in the results of this research and technology. The potential individual conflict of interest has been reviewed and managed by the University of Texas at Dallas, and it played no role in the study design; the collection, analysis, and interpretation of data; the writing of the article; or the decision to submit the article for publication. The funders had no role in the design of the study; in the collection, analyses, or interpretation of data; in the writing of the manuscript, or in the decision to publish the results.

References

1. Ganguly, A.; Rice, P.; Lin, K.-C.; Muthukumar, S.; Prasad, S. A Combinatorial Electrochemical Biosensor for Sweat Biomarker Benchmarking. *SLAS Technol.* **2019**, *25*, 25–32. [[CrossRef](#)] [[PubMed](#)]
2. Chapter 44. Prevention of Chronic Disease by Means of Diet and Lifestyle Changes. In *Disease Control Priorities in Developing Countries*, 2nd ed.; Oxford University Press: Washington, DC, USA, 2006.
3. Panjan, P.; Virtanen, V.; Sesay, A.M. Determination of Stability Characteristics for Electrochemical Biosensors via Thermally Accelerated Ageing. *Talanta* **2017**, *170*, 331–336. [[CrossRef](#)] [[PubMed](#)]
4. Ceren Ates, H.; Nguyen, P.Q.; Gonzalez-Macia, L.; Morales-Narváez, E.; Güder, F.; Collins, J.J.; Dincer, C. End-to-End Design of Wearable Sensors. *Nat. Rev. Mater.* **2022**, *7*, 887–907. [[CrossRef](#)] [[PubMed](#)]
5. Malhotra, B.D.; Ali, A. Nanomaterials in Biosensors: Fundamentals and Applications. In *Nanomaterials for Biosensors*; Elsevier: Amsterdam, The Netherlands, 2018; p. 1. [[CrossRef](#)]
6. Dhamu, V.N.; Banga, I.; Paul, A.; Ganguly, A.; Bhide, A.; Telang, C.; Muthukumar, S.; Prasad, S. Combinatorial Sensors: An Integrated Approach to Lifestyle Management and Environmental Surveillance. In *Reference Module in Biomedical Sciences*; Elsevier: Amsterdam, The Netherlands, 2021. [[CrossRef](#)]

7. Ozcelikay, G.; Bakirhan, N.K.; Ozkan, S.A. Novel Advances in Nanomaterial-Based Electrochemical Sensing of the Biomarker. In *The Detection of Biomarkers: Past, Present, and the Future Prospects*; Academic Press: Cambridge, MA, USA, 2022; pp. 209–224. [[CrossRef](#)]
8. Carrasco, S. Metal-Organic Frameworks for the Development of Biosensors: A Current Overview. *Biosensors* **2018**, *8*, 92. [[CrossRef](#)]
9. Moosavi, S.M.; Nandy, A.; Jablonka, K.M.; Ongari, D.; Janet, J.P.; Boyd, P.G.; Lee, Y.; Smit, B.; Kulik, H.J. Understanding the Diversity of the Metal-Organic Framework Ecosystem. *Nat. Commun.* **2020**, *11*, 4068. [[CrossRef](#)]
10. Li, H.; Eddaoudi, M.; O’Keeffe, M.; Yaghi, O.M. Design and Synthesis of an Exceptionally Stable and Highly Porous Metal-Organic Framework. *Nature* **1999**, *402*, 276–279. [[CrossRef](#)]
11. Makiura, R.; Motoyama, S.; Umemura, Y.; Yamanaka, H.; Sakata, O.; Kitagawa, H. Surface Nano-Architecture of a Metal–Organic Framework. *Nat. Mater.* **2010**, *9*, 565–571. [[CrossRef](#)]
12. Sutrisna, P.D.; Savitri, E.; Himma, N.F.; Prasetya, N.; Wenten, I.G. Current Perspectives and Mini Review on Zeolitic Imidazolate Framework-8 (ZIF-8) Membranes on Organic Substrates. *IOP Conf. Ser. Mater. Sci. Eng.* **2019**, *703*, 012045. [[CrossRef](#)]
13. García-Palacín, M.; Martínez, J.I.; Paseto, L.; Deacon, A.; Johnson, T.; Malankowska, M.; Téllez, C.; Coronas, J. Sized-Controlled ZIF-8 Nanoparticle Synthesis from Recycled Mother Liquors: Environmental Impact Assessment. *ACS Sustain. Chem. Eng.* **2020**, *8*, 2973–2980. [[CrossRef](#)] [[PubMed](#)]
14. Song, X.; Ou, Z.; Hu, X.; Zhang, X.; Lin, M.; Wen, L.; Li, M. Revealing Structure Properties of ZIF-8 Particles Prepared by Wet Chemical Etching via 3D Electron Tomography. *ACS Mater. Lett.* **2021**, *3*, 171–178. [[CrossRef](#)]
15. Mu, L.; Liu, B.; Liu, H.; Yang, Y.; Sun, C.; Chen, G. A Novel Method to Improve the Gas Storage Capacity of ZIF-8. *J. Mater. Chem.* **2012**, *22*, 12246. [[CrossRef](#)]
16. Zhao, Y.; Wei, Y.; Lyu, L.; Hou, Q.; Caro, J.; Wang, H. Flexible Polypropylene-Supported ZIF-8 Membranes for Highly Efficient Propene/Propane Separation. *J. Am. Chem. Soc.* **2020**, *142*, 20915–20919. [[CrossRef](#)] [[PubMed](#)]
17. Xue, W.; Zhou, Q.; Li, F.; Ondon, B.S. Zeolitic Imidazolate Framework-8 (ZIF-8) as Robust Catalyst for Oxygen Reduction Reaction in Microbial Fuel Cells. *J. Power Sources* **2019**, *423*, 9–17. [[CrossRef](#)]
18. Lu, G.; Hupp, J.T. Metal–Organic Frameworks as Sensors: A ZIF-8 Based Fabry–Pérot Device as a Selective Sensor for Chemical Vapors and Gases. *J. Am. Chem. Soc.* **2010**, *132*, 7832–7833. [[CrossRef](#)]
19. Wang, Q.; Sun, Y.; Li, S.; Zhang, P.; Yao, Q. Synthesis and Modification of ZIF-8 and Its Application in Drug Delivery and Tumor Therapy. *RSC Adv.* **2020**, *10*, 37600–37620. [[CrossRef](#)]
20. Bergaoui, M.; Khalfaoui, M.; Awadallah-F, A.; Al-Muhtaseb, S. A Review of the Features and Applications of ZIF-8 and Its Derivatives for Separating CO₂ and Isomers of C₃- and C₄- Hydrocarbons. *J. Nat. Gas. Sci. Eng.* **2021**, *96*, 104289. [[CrossRef](#)]
21. Poddar, A.; Conesa, J.J.; Liang, K.; Dhakal, S.; Reineck, P.; Bryant, G.; Pereiro, E.; Ricco, R.; Amenitsch, H.; Doonan, C.; et al. Encapsulation, Visualization and Expression of Genes with Biomimetically Mineralized Zeolitic Imidazolate Framework-8 (ZIF-8). *Small* **2019**, *15*, e1902268. [[CrossRef](#)]
22. Maddigan, N.K.; Tarzia, A.; Huang, D.M.; Sumbly, C.J.; Bell, S.G.; Falcaro, P.; Doonan, C.J. Protein Surface Functionalisation as a General Strategy for Facilitating Biomimetic Mineralisation of ZIF-8. *Chem. Sci.* **2018**, *9*, 4217–4223. [[CrossRef](#)] [[PubMed](#)]
23. Wei, T.H.; Wu, S.H.; Huang, Y.D.; Lo, W.S.; Williams, B.P.; Chen, S.Y.; Yang, H.C.; Hsu, Y.S.; Lin, Z.Y.; Chen, X.H.; et al. Rapid Mechanochemical Encapsulation of Biocatalysts into Robust Metal–Organic Frameworks. *Nat. Commun.* **2019**, *10*, 5002. [[CrossRef](#)]
24. Taghizadeh, T.; Ameri, A.; Talebian-Kiakalaieh, A.; Mojtabavi, S.; Ameri, A.; Forootanfar, H.; Tarighi, S.; Faramarzi, M.A. Lipase@zeolitic Imidazolate Framework ZIF-90: A Highly Stable and Recyclable Biocatalyst for the Synthesis of Fruity Banana Flavour. *Int. J. Biol. Macromol.* **2020**, *166*, 1301–1311. [[CrossRef](#)]
25. Cánovas, R.; Cuartero, M.; Crespo, G.A. Modern Creatinine (Bio)Sensing: Challenges of Point-of-Care Platforms. *Biosens. Bioelectron.* **2019**, *130*, 110–124. [[CrossRef](#)] [[PubMed](#)]
26. Dong, Y.; Liu, Y.; Lv, J.; Yang, L.; Cui, Y. Advancements in Amperometric Biosensing Instruments for Creatinine Detection: A Critical Review. *IEEE Trans. Instrum. Meas.* **2023**, *72*, 4006915. [[CrossRef](#)]
27. Chen, J.C.; Kumar, A.S.; Chung, H.H.; Chien, S.H.; Kuo, M.C.; Zen, J.M. An Enzymeless Electrochemical Sensor for the Selective Determination of Creatinine in Human Urine. *Sens. Actuators B Chem.* **2006**, *115*, 473–480. [[CrossRef](#)]
28. Han, P.; Xu, S.; Feng, S.; Hao, Y.; Wang, J. Direct Determination of Creatinine Based on Poly(Ethyleneimine)/Phosphotungstic Acid Multilayer Modified Electrode. *Talanta* **2016**, *151*, 114–118. [[CrossRef](#)] [[PubMed](#)]
29. Shaidarova, L.G.; Chelnokova, I.A.; Ilina, M.A.; Leksina, Y.A.; Gedmina, A.V.; Budnikov, H.K. Amperometric Detection of Creatinine and Uric Acid at the Screen-Printed Electrode Modified by Gold Nanoparticles in Flow-Injection Analysis. *Res. J. Pharm. Biol. Chem. Sci.* **2015**, *6*, 1629–1635.
30. Jayasekhar Babu, P.; Tirkey, A.; Mohan Rao, T.J.; Chanu, N.B.; Lalchandama, K.; Singh, Y.D. Conventional and Nanotechnology Based Sensors for Creatinine (A Kidney Biomarker) Detection: A Consolidated Review. *Anal. Biochem.* **2022**, *645*, 114622. [[CrossRef](#)] [[PubMed](#)]
31. Wang, A.B.; Fang, P.H.; Chu Su, Y.; Hsieh, Y.W.; Lin, C.W.; Chen, Y.T.; Hsu, Y.C. A Novel Lab-on-a-Chip Design by Sequential Capillary-Gravitational Valves for Urinary Creatinine Detection. *Sens. Actuators B Chem.* **2016**, *222*, 721–727. [[CrossRef](#)]
32. Rakesh Kumar, R.K.; Shaikh, M.O.; Chuang, C.H. A Review of Recent Advances in Non-Enzymatic Electrochemical Creatinine Biosensing. *Anal. Chim. Acta* **2021**, *1183*, 338748. [[CrossRef](#)] [[PubMed](#)]
33. Ruedas-Rama, M.J.; Hall, E.A.H. Analytical Nanosphere Sensors Using Quantum Dot-Enzyme Conjugates for Urea and Creatinine. *Anal. Chem.* **2010**, *82*, 9043–9049. [[CrossRef](#)] [[PubMed](#)]

34. Yue-dong, Y. Simultaneous Determination of Creatine, Uric Acid, Creatinine and Hippuric Acid in Urine by High Performance Liquid Chromatography. *Biomed. Chromatogr.* **1998**, *12*, 47–49. [[CrossRef](#)]
35. del Campo, G.; Irastorza, A.; Casado, J.A. Spectrophotometric Simultaneous Determination of Creatinine and Creatine by Flow Injection with Reagent Injection. *Fresenius J. Anal. Chem.* **1995**, *352*, 557–561. [[CrossRef](#)]
36. Pundir, C.S.; Kumar, P.; Jaiwal, R. Biosensing Methods for Determination of Creatinine: A Review. *Biosens. Bioelectron.* **2019**, *126*, 707–724. [[CrossRef](#)]
37. Lad, U.; Khokhar, S.; Kale, G.M. Electrochemical Creatinine Biosensors. *Anal. Chem.* **2008**, *80*, 7910–7917. [[CrossRef](#)]
38. Narimani, R.; Esmaili, M.; Rasta, S.H.; Khosroshahi, H.T.; Mobed, A. Trend in Creatinine Determining Methods: Conventional Methods to Molecular-Based Methods. *Anal. Sci. Adv.* **2020**, *2*, 308–325. [[CrossRef](#)]
39. Nan, M.N.; Bi, Y.; Xue, H.L.; Long, H.T.; Xue, S.L.; Pu, L.M.; Prusky, D. Modification Performance and Electrochemical Characteristics of Different Groups of Modified Aptamers Applied for Label-Free Electrochemical Impedimetric Sensors. *Food Chem.* **2021**, *337*, 127761. [[CrossRef](#)]
40. Ganguly, A.; Lin, K.C.; Muthukumar, S.; Prasad, S. Autonomous, Real-Time Monitoring Electrochemical Aptasensor for Circadian Tracking of Cortisol Hormone in Sub-Microliter Volumes of Passively Eluted Human Sweat. *ACS Sens.* **2020**, *6*, 63–72. [[CrossRef](#)]
41. Bard, A.J.; Faulkner, L.R. *Electrochemical Methods Fundamentals and Applications*, 2nd ed.; John Wiley & Sons: Hoboken, NJ, USA, 2001.
42. Scholz, F. *Electroanalytical Methods: Guide to Experiments and Applications*; Springer: Berlin/Heidelberg, Germany, 2010; ISBN 9783642029141.
43. Daniels, J.S.; Pourmand, N. Label-Free Impedance Biosensors: Opportunities and Challenges. *Electroanalysis* **2007**, *19*, 1239–1257. [[CrossRef](#)] [[PubMed](#)]
44. Randviir, E.P.; Banks, C.E. Electrochemical Impedance Spectroscopy: An Overview of Bioanalytical Applications. *Anal. Methods* **2013**, *5*, 1098–1115. [[CrossRef](#)]
45. Sarigul, N.; Korkmaz, F.; Kurultak, İ. A New Artificial Urine Protocol to Better Imitate Human Urine. *Sci. Rep.* **2019**, *9*, 20159. [[CrossRef](#)]
46. Ganguly, A.; Ebrahimzadeh, T.; Zimmern, P.E.; De Nisco, N.J.; Prasad, S. Label Free, Lateral Flow Prostaglandin E2 Electrochemical Immunosensor for Urinary Tract Infection Diagnosis. *Chemosensors* **2021**, *9*, 271. [[CrossRef](#)]
47. Ganguly, A.; Ebrahimzadeh, T.; Zimmern, P.; De Nisco, N.J.; Prasad, S. Label-Free, Novel Electrofluidic Capacitor Biosensor for Prostaglandin E2 Detection toward Early and Rapid Urinary Tract Infection Diagnosis. *ACS Sens.* **2021**, *7*, 186–198. [[CrossRef](#)] [[PubMed](#)]

Disclaimer/Publisher’s Note: The statements, opinions and data contained in all publications are solely those of the individual author(s) and contributor(s) and not of MDPI and/or the editor(s). MDPI and/or the editor(s) disclaim responsibility for any injury to people or property resulting from any ideas, methods, instructions or products referred to in the content.